

# Heat and fluid flow in complex joints during gas metal arc welding—Part II: Application to fillet welding of mild steel

W. Zhang, C.-H. Kim, and T. DebRoy<sup>a)</sup>

*Department of Materials Science and Engineering, The Pennsylvania State University, University Park, Pennsylvania 16802*

(Received 11 November 2003; accepted 4 February 2004)

A numerical model described in part I [W. Zhang, C.-H. Kim, and T. DebRoy, *J. Appl. Phys.* **95**, 5210 (2004)] was used to investigate the heat transfer and free surface flow during gas metal arc fillet welding of mild steel. Dimensional analysis was used to understand the importance of heat transfer by conduction and convection and the role of various driving forces on convection in the liquid weld pool. The calculated shape and size, finger penetration characteristic and solidified surface profile of the fillet welds were in fair agreement with the experimental results for various welding conditions. The calculated cooling rates were also in good agreement with independent experimental data. The effect of welding parameters on important weld bead characteristics was quantitatively studied using the numerical model. The results reported here indicate a significant promise for understanding and control of gas metal arc fillet welding processes based on fundamental principles of transport phenomena. © 2004 American Institute of Physics.

[DOI: 10.1063/1.1699486]

## I. INTRODUCTION

Gas metal arc (GMA) fillet welding is often regarded as one of the most useful yet highly complicated welding processes.<sup>1</sup> The complexities of fillet welding lie in the presence of a V-groove joint geometry, significant deformation of the free weld pool surface, the addition of metal droplets from a consumable electrode, and simultaneous occurrence of various important physical processes. These processes include the absorption of arc energy, the melting and the formation of the weld pool, the liquid metal circulation in the deformed pool, the transport of heat in the entire weldment, and the solidification of the molten metal.<sup>1-3</sup> All these features must be taken into account to accurately model the GMA fillet welding processes. With the advancements of computational hardware and software, it has now become practical to relax some of the simplifying assumptions of the previous research and address more realistic situations.

It should be noted that in our earlier work, a numerical heat conduction model employing a boundary fitted curvilinear coordinate system was used to study temperature fields in the complex fillet weld considering the deformation of the weld pool surface.<sup>4</sup> The model takes into account several special features during GMA fillet welding, which include complex fillet weld geometry, the significant deformation of the pool surface, and the transport of metal droplets into the weld pool that is largely responsible for the finger penetration commonly observed in the fusion zone. An enhanced thermal conductivity was assigned to the liquid metal to account the convective heat transfer in the weld pool. Although the heat conduction model reasonably predicted the weld bead geometry and cooling rates,<sup>4</sup> it was unable to describe the liquid metal convection and the resulting convective heat transfer in the pool. It has been well established that convec-

tion is usually the dominant mode of heat transfer in the weld pool and determines the weld temperature distribution and bead shape.<sup>3</sup> Recently, the effect of various driving forces on liquid metal convection has been examined. Examples include the liquid flow driven by the surface tension gradient, electromagnetic, and buoyancy forces.<sup>5-7</sup> Especially, the surface tension driving flow was found to be very effective in dissipation of the incident energy flux on the pool surface and often determine the weld pool geometry. For example, a liquid flow with negative temperature coefficient of surface tension often results in a wide and shallow pool. However, when some surface active elements are presented in the material, the temperature coefficient of surface tension may become positive<sup>8</sup> and the liquid flow pattern can be dramatically altered, which results in narrow and deep pool.<sup>9</sup> Such effect of surface active elements on the bead geometry could be readily understood considering liquid metal flow, while it poses real difficulty when using a heat conduction model with enhanced thermal conductivity of liquid metal. Hence, the knowledge of liquid metal flow in the weld pool is essential to complete understanding of welding processes.

In part I of this research work, a three-dimensional numerical model is developed to investigate the heat transfer, fluid flow, and the solidified surface profile during GMA fillet welding. The model uses a boundary fitted coordinate system to accurately calculate temperature and velocity fields in the complex physical domain considering deformation of the weld pool surface. The additional heat from the metal droplets is modeled considering the available knowledge base of the interaction between the droplets and the pool. The free surface profile is calculated by minimizing the total free surface energy considering the additional filler metal. In this article, the effect of liquid metal convection on the heat transfer, the role of individual driving forces, and the resulting pool geometry are investigated. In particular, the calculated fusion zone shape and size, finger penetration, and

<sup>a)</sup>Electronic mail: debroy@psu.edu

TABLE I. Welding conditions used in the GMA fillet welding experiments.

Case No.	Contact tube to workpiece distance (mm)	Wire feeding rate (mm/s)	Travel speed (mm/s)	Voltage (V)	Current (A)
1	22.2	169.3	4.2	31	312.0
2	22.2	211.7	6.4	31	362.0
3	22.2	169.3	6.4	33	312.0
4	22.2	211.7	4.2	33	362.0
5	28.6	169.3	6.4	31	286.8
6	28.6	169.3	4.2	33	286.8
7	28.6	211.7	4.2	31	331.4
8	28.6	211.7	6.4	33	331.4

Polarity: Direct current electrode positive  
 Joint type: Fillet joint, flat position, 90° joint angle, and no root gap  
 Electrode type: AWS E70S-6, 1.32 mm (0.052 in.) diameter solid wire.  
 Base metal: ASTM A-36 mild steel  
 Shielding gas: Ar-10% CO<sub>2</sub>  
 Droplet transfer: Spray transfer mode

cooling rates were compared with the corresponding experimental results for various welding conditions.

## II. RESULTS AND DISCUSSION

The numerical heat transfer and fluid flow model was used for the calculation of temperature and velocity fields for the eight cases listed in Table I. The welding conditions used for these fillet welding experiments are also given in this table. The material properties for the A-36 steel workpiece<sup>4</sup> and the other data used in the calculations are presented in Table II.

### A. Convection versus conduction on the weld temperature distribution

#### 1. Dimensionless analysis

During welding, the arc energy is transported from the top surface of the weld pool to the surrounding solid region

TABLE II. Physical properties of the A-36 steel and the other data used in the calculation.<sup>a</sup>

Name	Value
Liquidus temperature, $T_l$ , (K)	1785.0
Solidus temperature, $T_s$ , (K)	1745.0
Density of metal, $\rho$ , (kg m <sup>-3</sup> )	7800
Thermal conductivity of solid, $k_s$ , (J m <sup>-1</sup> ·s <sup>-1</sup> ·K <sup>-1</sup> )	21.0
Enhanced thermal conductivity of liquid, $k_l$ , (J m <sup>-1</sup> ·s <sup>-1</sup> ·K <sup>-1</sup> )	88.2
Enhanced viscosity of liquid metal, $\mu$ , (kg m <sup>-1</sup> s <sup>-1</sup> )	$3 \times 10^{-2}$
Specific heat of solid, $C_{ps}$ , (J kg <sup>-1</sup> ·K <sup>-1</sup> )	703.4
Specific heat of liquid, $C_{pl}$ , (J kg <sup>-1</sup> ·K <sup>-1</sup> )	808.1
Surface tension of liquid metal at melting point, $\gamma$ , (N m <sup>-1</sup> )	1.2
Temperature coefficient of surface tension, $d\gamma/dT$ , (N m <sup>-1</sup> ·K <sup>-1</sup> )	$-0.35 \times 10^{-4}$
Magnetic permeability, $\mu_m$ , (N A <sup>-2</sup> )	$1.26 \times 10^{-6}$
Coefficient of thermal expansion, $\beta$ , (K <sup>-1</sup> )	$1.0 \times 10^{-5}$
Arc efficiency, $\eta$	54%
Arc radius, $r_b$ , (mm)	5.0
Convective heat transfer coefficient, $h_c$ , (W mm <sup>-2</sup> K <sup>-1</sup> )	42.0
Emissivity, $\epsilon$	0.7
Ambient temperature, $T_a$ , (K)	298

<sup>a</sup>See Ref. 4

by both heat conduction and liquid metal convection. The rate of the heat flow determines not only the peak temperature and shape of the weld pool but also the temperature distribution in the heat-affected zone (HAZ). Therefore, it is important to understand the effects of conduction and convection on the heat dissipation in the weld pool. The relative importance of convection versus conduction in transferring heat in the pool can be accessed from the value of the Peclet number (Pe), which is given by

$$Pe = \frac{u_R \rho C_{pl} L_R}{k_l} \tag{1}$$

where  $u_R$  and  $L_R$  are the characteristic velocity and length of the weld pool, respectively, and the symbols  $\rho$ ,  $C_{pl}$ , and  $k_l$  are density, specific heat, and thermal conductivity of liquid metal, respectively. When Pe is large, which in physical terms means large liquid metal velocity, large weld pool, and poor thermal conductivity, the liquid metal convection significantly affects the heat transfer in the weld pool. On the other hand, when Pe is small, say much less than unity, the conduction plays an important role in the heat dissipation in the pool.

Figure 1 shows the calculated temperature and velocity fields in a fillet weld. The welding conditions used are those in case No. 4 shown in Table I. For clarity, only half of the workpiece is shown, since the weld is symmetric about the central longitudinal plane containing the welding direction. For the fillet weld shown in Fig. 1, if the average  $v$  velocity and the pool width are used as the characteristic velocity and length of the weld pool, respectively, the Peclet number is calculated to be about 120. Since the Peclet number is much larger than unity, the liquid metal convection plays a dominant role in dissipating the heat in the weld pool. In other words, a model, which takes into account only the conduction heat transfer in the pool, is not able to accurately describe the heat transport process in the fillet weld.

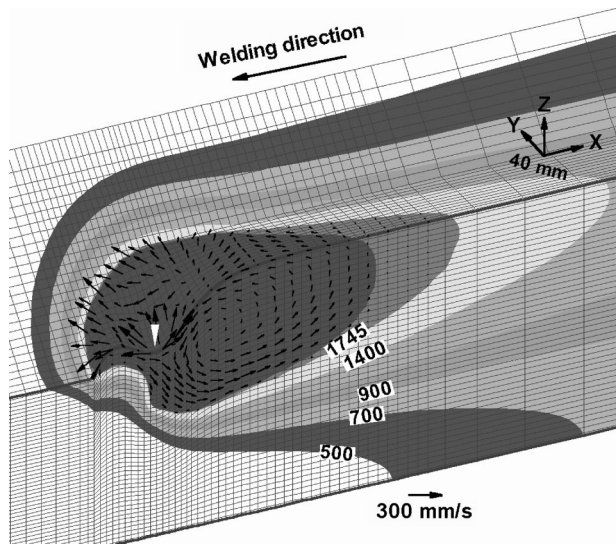


FIG. 1. Calculated temperature and velocity fields in a fillet weld. All the temperatures are given in Kelvin. The white arrow in the middle of the weld pool indicates the location of the heat source. The weld pool boundary is represented by the 1745 K isothermal line. Welding conditions used are those given in case No. 4.

**2. Convection versus conduction on the temperature distribution in the weld pool and HAZ**

To understand the role of liquid metal convection, weld temperature distributions were calculated using the same welding parameters with and without considering convection. In other words, the effect of convection was ignored in one calculation and considered in the other. Figure 2 shows the calculated temperature field at the weld top surface for two cases: one with convection (i.e., heat transfer and fluid flow calculation), and the other without convection (i.e., heat conduction calculation). As shown in Fig. 2, in front of the heat source, the weld pool boundary, represented by the 1745 K isothermal line, expands slightly outward for the case with convection, since the liquid metal flow helps carry heat away from the center to the front boundary. In the solid region ahead of the heat source, the difference in the isotherms between two cases is rather small. This small difference is expected since the isotherms in front of the heat source are largely compressed due to the motion of the heat source

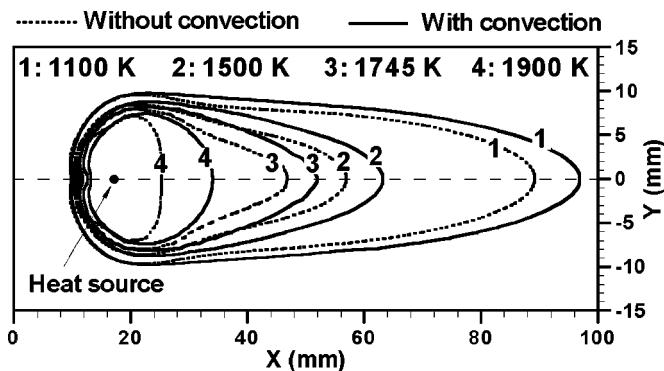


FIG. 2. Calculated temperature distributions at the weld top surface for cases with and without considering convection. Welding conditions are the same as those in Fig. 1.

TABLE III. Effect of different driving forces on the weld pool characteristics. Symbol  $T_{peak}$  represents the peak temperature of the weld pool, while symbols  $u_{max}$ ,  $v_{max}$ , and  $w_{max}$  represent the maximum velocity (magnitude) in  $x$ ,  $y$ , and  $z$  directions, respectively.

	$T_{peak}$ (K)	$u_{max}$ (mm/s)	$v_{max}$ (mm/s)	$w_{max}$ (mm/s)	Width (mm)	Depth (mm)
Conduction	2730	0	0	0	17.0	13.2
All three driving forces	2380	352	349	210	17.0	14.0
Marangoni stress	2320	425	382	236	18.3	13.0
Buoyancy force	2700	6.7	6.1	5.7	17.0	13.1
Electromagnetic force	2250	178	177	218	15.4	15.6

(welding speed). As a result, the heating rates are expected to be similar for cases with or without the convection calculation. On the other hand, the isotherms are quite different behind the heat source for the two cases. As shown in Fig. 2, the isotherms are elongated for the case with convection than the one without convection, since the melt convection brings a significant amount of heat energy to the rear part of the weld pool. Therefore, the cooling rates for the case considering convection are expected to be smaller than those without considering convection.

Table III summarizes some characteristic parameters of the fillet weld pool calculated for various cases. As shown in this table, the peak temperature of the weld pool for the case without convection is 350 K higher than that for the case considering convection. The higher computed peak temperature in the absence of convection is expected, since the liquid metal convection plays a major role in dissipating heat in the weld pool. For the case without convection, the heat dissipation in the pool relies solely on the conduction of heat. Thus, the heat dissipation rate for this case is much slower than the case with convection. Hence, more heat is accumulated in the weld pool and the peak temperature in the weld pool is higher for the case without convection.

**3. Convection versus conduction on the weld bead shape**

Figure 3 shows the comparison of the weld bead shape for two cases with and without considering convection. As shown in this figure, the weld bead for case with convection is narrower than that without convection. In other words, the weld bead profile is more rounded for the case without con-

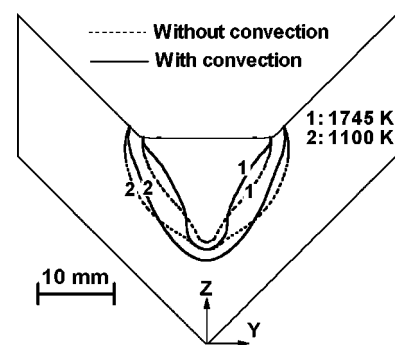


FIG. 3. Comparison of weld bead geometry for cases with and without convection. Welding conditions are the same as those in Fig. 1.

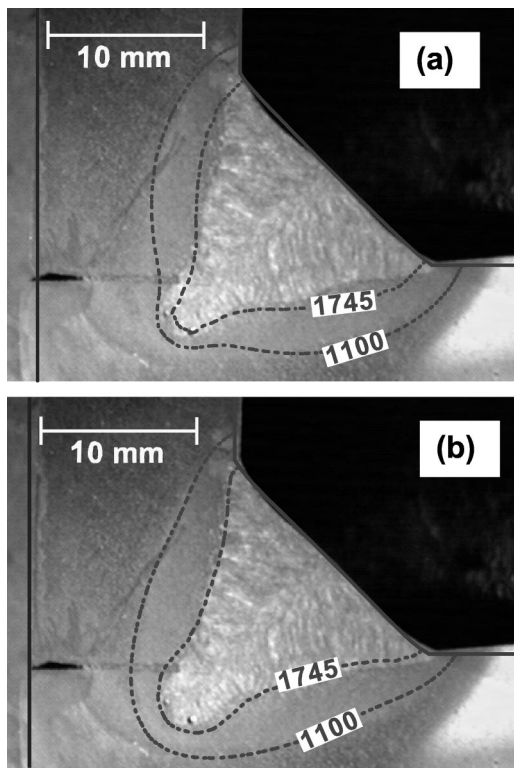


FIG. 4. Comparison between the calculated and measured weld bead profile: (a) using the heat conduction model with an effective thermal conductivity of  $420 \text{ J m}^{-1} \text{ s}^{-1} \text{ K}^{-1}$ ,<sup>4</sup> and (b) using the heat transfer and fluid flow model with an effective thermal conductivity of  $88.2 \text{ J m}^{-1} \text{ s}^{-1} \text{ K}^{-1}$ . All other input parameters used in the two models are the same. Welding conditions are the same as those in Fig. 1.

vection, which is due to the fact that the rate of heat conduction is the same in all directions. Figure 3 also indicates that the depth of the floating zone (FZ) is deeper for the case with convection. As shown in Fig. 1, the liquid metal is driven downwards in the middle of the weld pool by the electromagnetic force. This strong downward flow is responsible for the deeper penetration in the case with convection.

It should be noted that in our previous work, we used a heat conduction model, which does not take into account the liquid metal convection, to calculate the weld temperature fields and bead profile.<sup>4</sup> In that heat conduction model, an enhanced thermal conductivity of the liquid metal was used to account for the effect of convection on the heat dissipation in the weld pool. To match the width and depth of the weld bead measured experimentally, the value of the enhanced thermal conductivity used in the calculation was  $420 \text{ J m}^{-1} \text{ s}^{-1} \text{ K}^{-1}$ .<sup>4</sup> This value is about 20 times higher than the actual value of the thermal conductivity of liquid metal, which is equal to  $21 \text{ J m}^{-1} \text{ s}^{-1} \text{ K}^{-1}$ . In our present heat transfer and fluid model, a value of  $88.2 \text{ J m}^{-1} \text{ s}^{-1} \text{ K}^{-1}$  was used for the enhanced thermal conductivity. The enhancement is to take into account the effect of turbulence in the weld pool. Figure 4 shows the calculated weld bead profiles, which fit the experimental bead profile best, using two models. As shown in this figure, the calculation considering convection [Fig. 4(b)] results in a better agreement with the overall experimental bead profile than the one without convection [Fig. 4(a)]. In other words, although a heat conduction model can

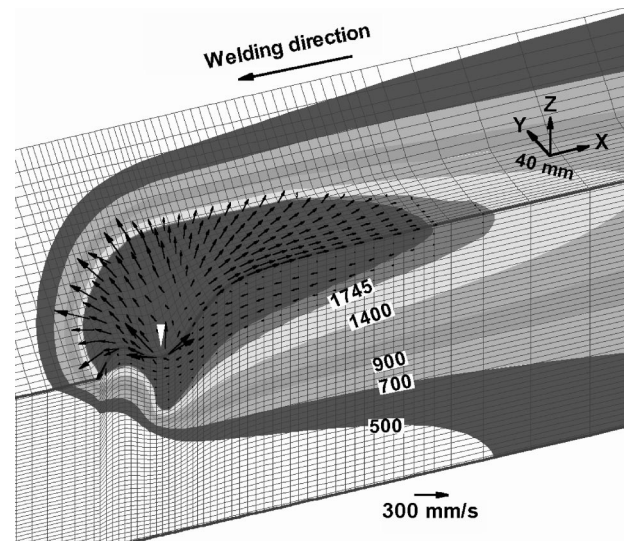


FIG. 5. Marangoni convection with an outward surface flow in a fillet weld pool. The white arrow indicates the location of the heat source. All the temperatures are given in Kelvin. Welding conditions used are those in case No. 4.

simulate the effect of convection by introducing a very high value of thermal conductivity of liquid metal, it is still not possible for it to accurately predict the weld bead geometry. The heat transfer and fluid flow model, although it also relies on the use of the enhanced thermal conductivity to simulate turbulence flow, provides a more realistic description of the physical processes during fillet welding, and thus results in a better prediction of the weld bead profile.

## B. Role of driving forces on the liquid metal convection and the weld pool shape

During arc welding, more than one type of driving forces act on the liquid metal in the weld pool. Therefore, the fluid flow pattern in the weld pool is a result of a combination of various driving forces. In the present study, three primary driving forces, namely the electromagnetic force, the Marangoni shear stress and the buoyancy force were considered in the calculations.

The effect of various driving forces on the liquid metal convection and the resulting weld pool shape have been extensively studied for welding of butt joints, i.e., simple rectangular workpiece. However, for welding of fillet joints with complex geometry, the study of the role of the driving forces remains scarce. Since it is rather difficult to separate the effect of the individual driving forces by conducting welding experiments, the numerical heat transfer and fluid flow model and dimensionless analysis were employed to examine their role in fillet welds.

### 1. Marangoni convection

In butt welds, the Marangoni convection with a negative  $d\gamma/dT$  results in a liquid flow from the center to the periphery at the weld pool top surface and upward flow at the center of the pool.<sup>1,4,10</sup> Figure 5 shows the temperature and velocity fields in a fillet weld in the absence of electromagnetic and buoyancy forces. As shown in this figure, the effect

of Marangoni shear stress in the fillet weld is similar to that in butt welds. Since the value of  $d\gamma/dT$  is negative for the A-36 steel, the warmer liquid metal has a lower surface tension and vice versa. At the pool top surface, the liquid metal is flowing radically outward, since the warmer liquid metal of lower surface tension near the center of the pool is pulled outward by the cooler metal of higher surface tension at the pool edge. Pushed by the strong outward flow at the top surface, the liquid metal is transported outwards from the middle of the weld pool and arises at the center of the pool. Therefore, along the central longitudinal plane, a clockwise circulation loop is formed behind the heat source while anticlockwise circulation loop exists in front of the heat source, as shown in Fig. 5. The anticlockwise circulation is much weaker than the clockwise one behind the heat source. This is because the weld pool is largely compressed in front of the heat source due to the welding speed and the arc pressure, and the liquid flow is significantly restricted there. The compressed weld pool in front of the heat source also constrains the liquid flow resulting from other two driving forces, i.e., the buoyancy and electromagnetic forces, as shown in the following sections.

An order of magnitude of the maximum velocity ( $u_{st}$ ) under Marangoni convection can be estimated by from following expression:<sup>3</sup>

$$u_{st}^{3/2} = \frac{\Delta T}{0.664(\rho\mu W)^{1/2}} \left| \frac{d\gamma}{dT} \right|, \quad (2)$$

where  $\Delta T$  is the temperature difference between the peak pool temperature and solidus temperature, and  $W$  is the width of the weld pool. Using Eq. (2) and the physical property data given in Table II, the maximum velocity is estimated to be of the order of 280 mm/s. This value agrees fairly well with that calculated using the heat transfer and fluid flow model, where the maximum velocity was found to be around 420 mm/s. Furthermore, as shown in Fig. 5, the maximum velocity is found to be located in front of the heat source at the top surface of the weld pool, since the temperature gradient ahead of the heat source is much higher than that behind it.

Using Eq. (1), the Pelect number is found to be around 140 under the effect of Marangoni convection. Therefore, the heat transfer by convection is the dominant mechanism of the heat dissipation in the weld pool, and the convective heat transfer determines the pool shape. Table III summarizes some weld pool characteristic parameters under the Marangoni convection. As shown in this table, the weld pool is wide and shallow. The depth of the weld pool is even less than that for conduction case. This is because the arc energy input is largely carried away from the center to the periphery of the pool by the strong outward flow at the top surface. The upward flow in the middle of the pool hinders the heat transfer along the depth direction.

## 2. Buoyancy driven flow

The Boussinesq approximation was used in the calculation of buoyancy driven flow. In other words, the variation in the density of the liquid metal is ignored, except insofar as it

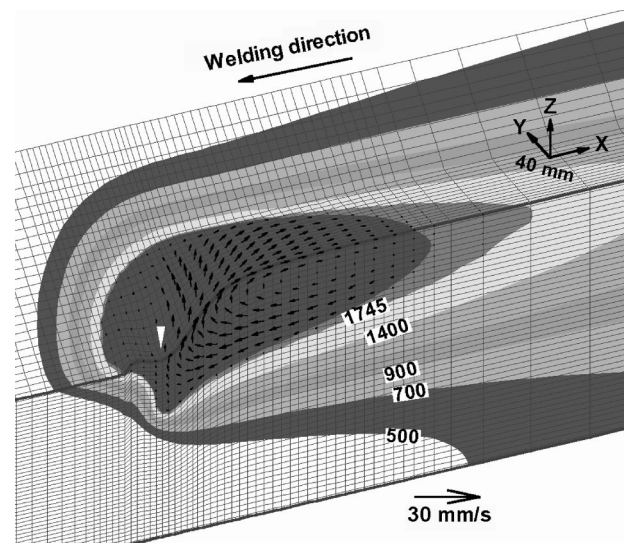


FIG. 6. Calculated temperature and velocity fields under the buoyancy driven convection. Welding conditions are the same as those in Fig. 5.

gives rise to a buoyancy force, which is also termed as the gravitational force. Figure 6 shows the calculated temperature and velocity fields under the buoyancy driven convection. It is found that the flow pattern driven by the buoyancy force in the fillet weld is similar to that in the butt welds. As shown in Fig. 6, the liquid metal rises along the pool center with low magnitude and fall along the pool boundary due to the local variation of density. This flow pattern is expected because the liquid metal near the heat source is at a relatively high temperature. It moves upwards because of its relatively low density. On the other hand, the liquid metal near the pool boundary has relatively low temperature and it flows downward because of its high density.<sup>11</sup> Figure 6 clearly indicates a clockwise circulation loop behind the heat source along the central longitudinal plane. The anticlockwise circulation loop in front of the heat source is much weaker due to the constraint of the weld pool there. Overall, the flow pattern resulted from the buoyancy force is similar to that resulted from the Marangoni shear stress, while with a much less magnitude of the flow velocity.

An order of magnitude of the maximum velocity ( $u_{grv}$ ) under the buoyancy driven flow is given by<sup>12</sup>

$$u_{grv} = \sqrt{g\beta\Delta TD}, \quad (3)$$

where  $g$  is the acceleration due to gravity,  $\beta$  is the thermal expansion coefficient, and  $D$  is the pool depth. Using Eq. (3), the order of the magnitude of the maximum velocity is estimated to be about 30 mm/s. The maximum velocity calculated using heat transfer and fluid flow model is around 7 mm/s, which is about the same order as the value estimated using Eq. (3).

For the buoyancy driven flow, the Pelect number calculated using Eq. (1) is found to be approximately 0.2. Therefore, the heat transfer by conduction is the dominant mechanism in the heat dissipation in the weld pool. In other words, the convection plays a much less important role in transferring the heat than the conduction does. As shown in Table III, due to the poor heat dissipation in the weld pool, the peak

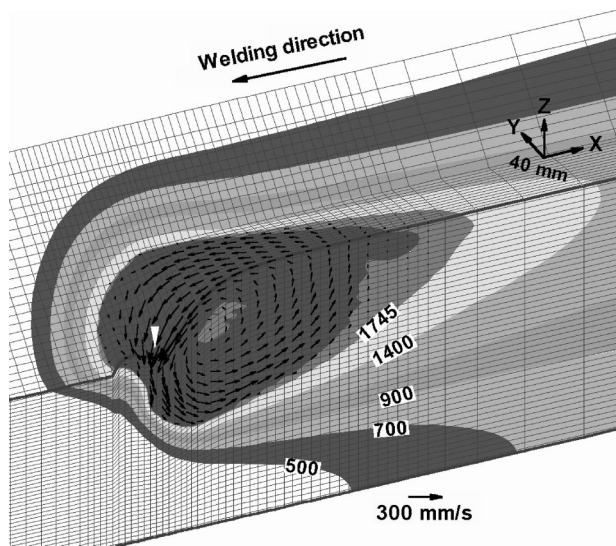


FIG. 7. Calculated temperature and velocity fields under the electromagnetic force driven convection. Welding conditions are the same as those in Fig. 5.

temperature of the pool under gravity driven flow is only slightly smaller than that of the conduction case. The weld pool shape is almost the same as that of the conduction case.

### 3. Flow driven by the electromagnetic force

The electromagnetic force, also called Lorentz Force, is caused by the electric current field together with the magnetic field it induces in the metal workpiece. Figure 7 shows the calculated temperature and velocity fields under electromagnetic convection in a fillet weld. As shown in this figure, the flow pattern is similar to that in butt welds. At the center of the weld pool, the liquid metal is driven downwards, whereas at the top surface the melt flows from the periphery to the center of the pool. As a result, a strong anticlockwise circulation loop is formed along the central longitudinal plane of the weld. This flow pattern is expected since the direction of the electromagnetic force is downward and inward. Figure 7 indicates that the flow pattern produced by the electromagnetic force is opposite to that induced by the Marangoni shear stress shown in Fig. 5.

As shown in Fig. 7, the maximum velocity due to the electromagnetic force is located in the middle of the weld pool along the central longitudinal plane. The maximum velocity is found to be 218 mm/s in the fillet weld pool. An order of magnitude calculation of the maximum velocity ( $u_{emf}$ ) under electromagnetic convection can be done by the following expression:<sup>12</sup>

$$u_{emf} = \frac{DI}{2\pi r_j^2} \sqrt{\frac{10\mu_m D}{\rho L_w}}, \quad (4)$$

where  $D$  is the depth of the weld pool,  $I$  is the current,  $r_j$  is the current distribution parameter (5 mm),  $\mu_m$  is the magnetic permeability,  $\rho$  is the density of the liquid metal, and  $L_w$  is the thickness of the workpiece. Using Eq. (4), the magnitude of the maximum velocity is estimated to be around 290 mm/s, which is in a good agreement with that calculated using the heat transfer and fluid flow model.

The Plect number for the flow driven by the electromagnetic force is found to be 70 for the fillet weld pool shown in Fig. 7. Therefore, the convection pattern has a strong influence on the heat transfer. The arc energy input is primarily carried from the surface towards the bottom of the weld pool by the downward flow in the middle of the weld pool. The heat energy is then dissipated into the solid region surrounding the weld pool as the flow arises along the pool boundary. Comparing with the weld pool for the Marangoni convection, the width of the pool is decreased while the depth is increased for electromagnetic convection, as shown in Table III.

### 4. Relative importance of the driving forces

In the foregoing discussion, the role of individual driving forces is examined. It is also important to know the relative importance of the driving forces on the liquid convection and the weld pool geometry. The following dimensionless numbers are used to evaluate the relative importance of the driving forces, as indicated in Eqs. (5a)–(5c).<sup>7,12</sup>

The ratio of buoyancy force to viscous force is determined by Grashof number

$$Gr = \frac{g\beta L_B^3 \Delta T \rho^2}{\mu^2}, \quad (5a)$$

where  $L_B$  is a characteristic length for the buoyancy force in the liquid pool, and is approximated by one eighth of the pool width.<sup>7</sup>

Magnetic Reynolds number defines the ratio of electromagnetic force to viscous force, and is expressed as

$$Rm = \frac{\rho \mu_m I^2}{4\pi^2 \mu^2}. \quad (5b)$$

Surface tension Reynolds number is used to describe the ratio of surface tension gradient force to viscous force, and is calculated as

$$Ma = \frac{\rho L_R \Delta T \left| \frac{d\gamma}{dT} \right|}{\mu^2}. \quad (5c)$$

Based on the temperature and velocity fields shown in Fig. 1 and the physical properties given in Table II, the dimensionless numbers were calculated. The value of  $Gr$ ,  $Rm$ , and  $Ma$  were calculated to be 12.0,  $3.6 \times 10^4$ , and  $2.9 \times 10^4$ , respectively. The relative importance of the driving forces, i.e., surface tension stress, electromagnetic and buoyancy forces, can thus be judged by the combination of these dimensionless numbers. For example, the ratio of the surface tension shear stress to the buoyancy force is expressed as

$$R_{S/B} = \frac{Ma}{Gr}, \quad (6)$$

while the ratio of the electromagnetic force to the buoyancy force is given by

$$R_{M/B} = \frac{Rm}{Gr}. \quad (7)$$

Based on the earlier calculate values of the dimensionless numbers,  $R_{S/B}$  is equal to  $2.3 \times 10^3$ , and  $R_{M/B}$  is equal to  $2.9 \times 10^3$ . Therefore, it is expected that the liquid flow is mainly driven by the Marangoni stress and electromagnetic force, and to a much less extent, by the buoyancy force. The relative importance of driving forces based on above dimensionless analysis is also consistent with the flow field obtained using the heat transfer and fluid flow model for individual driving forces shown Figs. 5, 6 and 7.

### 5. Combined effect of all the driving forces

The calculated temperature and velocity fields, when all three driving forces are presented, are shown in Fig. 1. As shown in this figure, the liquid metal motion is quite complicated due to the combined effect of the driving forces. The electromagnetic force plays a dominant role in driving the liquid metal flow in the weld pool. In the middle of the weld pool, the liquid metal is driven downwards by the electromagnetic force, and a major anticlockwise circulation loop is formed along the central longitudinal plane. On the other hand, at the top surface of the weld pool, the Marangoni shear stress drives the melt from the center to the edge of the pool in the region close to the heat source, where the spatial variation of the surface temperature is relatively high. In the rear part of the weld pool, where the temperature gradient is relatively low, the effect of Marangoni shear stress is less strong than that of electromagnetic force. As a result, the liquid metal flows inward in the rear part of the pool.

### C. Evolution of free surface profile

The evolution of the free surface profile for case No. 4 is illustrated in Fig. 1. As shown in this figure, the weld top surface is severely deformed under the arc heat source. The molten metal is pushed to the rear part of the weld pool by the arc force. As a result of the filler metal addition, the solidified weld metal forms pronounced weld reinforcement. The calculated temperature and velocity field and surface profile at various cross sections perpendicular to the welding direction for case No. 4 is shown in Fig. 8, where the weld pool boundary is represented by the 1745 K solidus isotherm of A-36 steel. Figure 8(a) shows a plane located 6 mm ahead of the heat source, where the base metal has not yet melted. The region directly under the heat source is shown in Fig. 8(b). The weld pool surface is severely depressed under the effect of the arc pressure, and the liquid metal flows downwards in the middle of the pool driven by the electromagnetic force. As the monitoring location moves away from the heat source, the weld pool surface shows considerably less depression as would be expected from the reduction in arc pressure. Furthermore, the accumulation of the liquid metal in the rear of the weld pool is clearly visible in Figs. 8(c) and 8(d). This accumulated liquid metal forms the weld reinforcement after solidification. The temperature profile shown in Figs. 8(b) and 8(c) also indicates the fillet weld pool with the characteristic shape of finger penetration during GMA welding.

It should be noted that the liquid metal at the top surface shown in Fig. 8(c) appears to move out of the weld pool. In

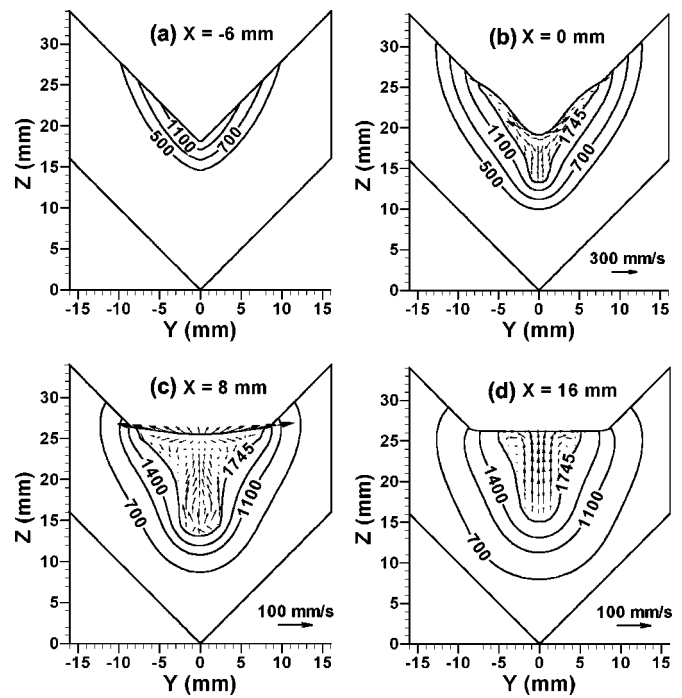


FIG. 8. Calculated temperature field at four different cross sections perpendicular to the welding direction. The temperatures are given in Kelvin. The  $X=0$  plane corresponds to the heat source location in this figure. Welding conditions are the same as those in case No. 4.

other words, the normal velocity to the pool top surface seems to be nonzero. This is due to the two-dimensional projection of the three dimensional velocity field is shown. As shown in Fig. 1, the normal velocity is zero at the top surface of the weld pool.

### D. Weld thermal cycles

The temperature field obtained from the calculation is at quasisteady state, since the coordinate system is attached to the heat source moving at a constant welding speed. Therefore, the thermal cycles can be calculated by converting the  $x$

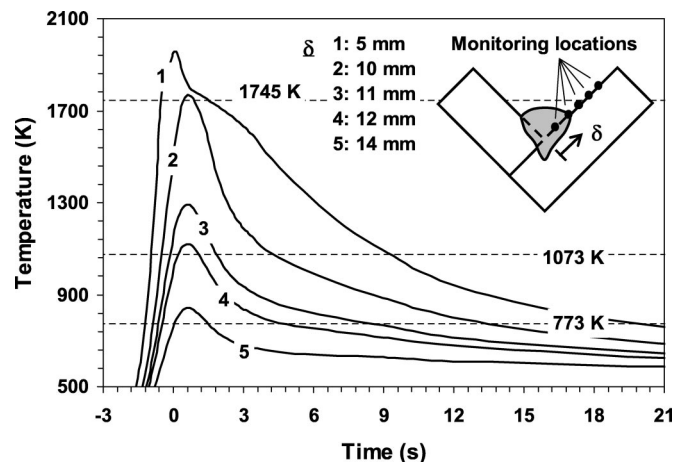


FIG. 9. Calculated thermal cycles in the fillet weld. Symbol  $\delta$  represents the distance from the joint root to a monitoring location at the top surface, as shown in the small figure. Time zero is arbitrarily set to be correspondent to  $X=0$  mm location.

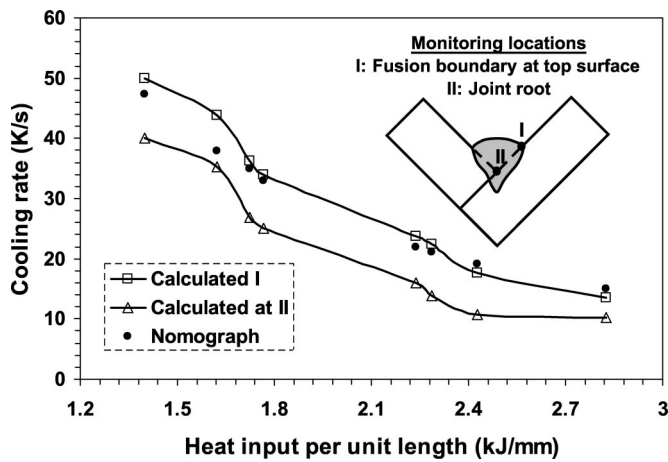


FIG. 10. Calculated average cooling rate  $\dot{T}_{8/5}$  at two monitoring locations in the fillet weld for various welding conditions. The solid dots represent the cooling rate estimated using the nomograph available in the literature (see Ref. 13).

distance into time using the welding speed. Figure 9 shows the thermal cycles at the top surface of the fillet weld for case No. 2. Curve 1 is located in the FZ. Curve 2 is located at the fusion boundary. All other curves are located in the HAZ. As shown in Fig. 9, the heating rates are much higher than the cooling rates. This is due to the following two reasons. First, the isotherms in front of the heat source are compressed whereas those behind it are largely elongated due to the high welding speed. Second, the existence of the volumetric heat source also contributes to the high heating rates. As expected, the peak temperatures are higher at locations close to the weld center, and decrease as the monitoring location moves outwards.

In welding of steels, the average cooling rate,  $\dot{T}_{8/5}$ , from 1073 to 773 K (800 to 500 °C) is of importance, since it affects the final microstructure of the weld metal for most steels.<sup>12</sup> Figure 10 shows the calculated average cooling rates at two monitoring locations, i.e., fusion boundary at the top surface and the joint root, for various welding conditions shown in Table I. As shown in this figure, the calculated average cooling rate decreases as the heat input per unit length (defined as the total power input/welding speed) increases. The effect of heat input per unit length on  $\dot{T}_{8/5}$  can be explained as follows. The average cooling rate  $\dot{T}_{8/5}$  is calculated as

$$\dot{T}_{8/5} = \frac{T_{800} - T_{500}}{t_{8/5}} = \frac{300U_w}{\Delta d_{8/5}}, \quad (8)$$

where  $t_{8/5}$  is the cooling time from 1073 to 773 K,  $U_w$  is the welding speed and  $\Delta d_{8/5}$  is the distance between two points where a line parallel to the  $x$  direction intercepts the 1073 and 773 K isothermal contours. Let us first consider the changes in the cooling rate resulting from an increase in welding speed. As the  $U_w$  increases, both the 1073 and 773 K isotherms expands outwards. However, the distance  $\Delta d_{8/5}$  does not change significantly. As a result, the cooling rate increases. Since an increase in  $U_w$  is accompanied by a reduction in the heat input per unit length, a reduction in heat

input is thus accompanied by an increase in the cooling rate, as observed in Fig. 10. On the other hand, when the welding speed is kept constant and the power input is increased, the isotherms are expanded and  $\Delta d_{8/5}$  also increases. Therefore, the cooling rate decreases for an increase in the power input. Since both a decrease in the welding speed and an increase in the power input result in a decline in the cooling rate, the higher the heat input per unit length, the lower the cooling rate  $\dot{T}_{8/5}$ .

Figure 10 also indicates that the average cooling rates at the joint root are smaller than those at the fusion boundary of the top surface. This is because the heat is conducted more easily at the top surface than at the central plane. In the literature, a cooling rate nomograph<sup>13</sup> is commonly used to estimate the average cooling rate  $\dot{T}_{8/5}$  for various welding conditions. As shown in Fig. 10, the calculated cooling rates at the fusion boundary agree reasonable well with those estimated using the nomograph. This good agreement indicates the validity of the fillet heat transfer and fluid flow model. Furthermore, the heat transfer and fluid flow model is capable to provide much more information on cooling rates than the nomograph, such as the spatial variation of the cooling rate.

### E. Weld bead geometry and the solidified surface profile

Figure 11 shows the calculated weld bead shape for all the eight cases listed in Table I. As shown in this figure, the calculated weld bead geometry for all cases agrees reasonably well with the corresponding experimental results. In particular, the shape of the weld reinforcement and the finger penetration could be satisfactorily predicted by the model. Comparing with the results calculated using the heat transfer model in our previous work,<sup>4</sup> the present heat transfer and fluid flow model provides a better agreement with the experimental weld bead profile. It should be noted that some discrepancy between the experimental bead profile and the computed results are observed in Figs. 11(c), 11(g), and 11(h). Part of this discrepancy is contributed by the thermal stress induced distortion, as can be evidenced by the gap between the two perpendicular plates.

Since the weld bead geometric characteristics are detrimental to the mechanical properties of the fillet weld, the effect of various welding parameters on the weld bead shape were studied. Figure 12 shows three important geometrical parameters of the weld bead, i.e., the leg length, penetration, and the actual throat as a function of the welding current. As shown in this figure, both the experimental data and the computed results show that the geometrical parameters increase with the current. Furthermore, the computed results and the experimental data show a reduction in all these dimensions with an increase in the welding speed. As shown in Fig. 13, these three geometric parameters are also plotted as a function of heat input per unit length. It is observed that only the leg length increases continuously with the increase in heat input. The data for the penetration and actual throat are segregated into clusters with identifiable welding speeds.

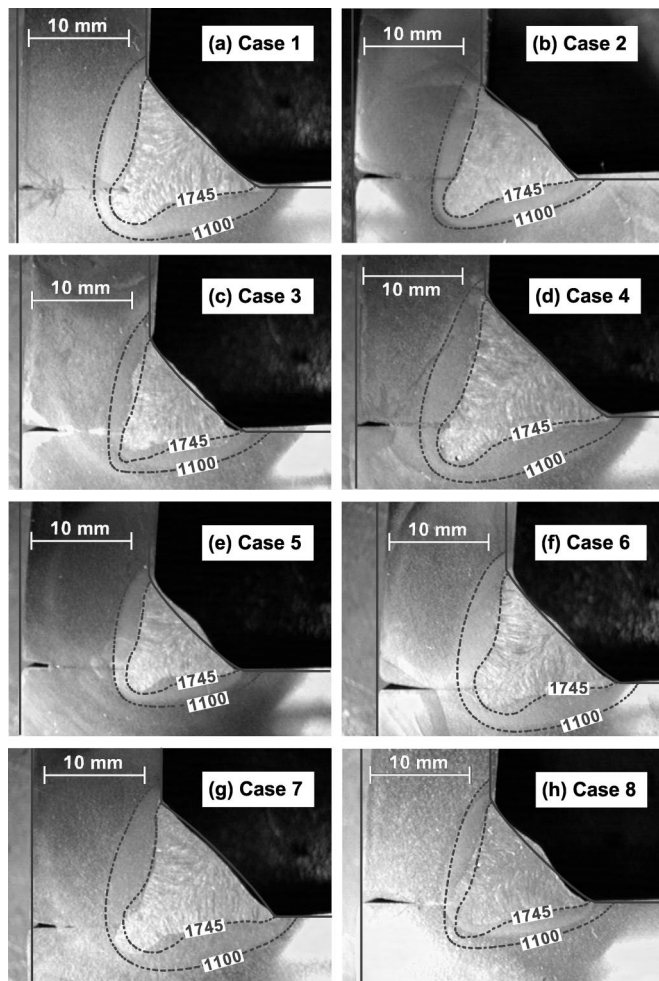


FIG. 11. Comparison between the calculated and experimental weld geometry for different cases given in Table I. The 1745 K solidus isotherm represents the calculated weld pool boundary.

Figures 12 and 13 indicate that the leg length depends strongly on the heat input per unit length, while the penetration is affected largely by the welding current. The dependence of the leg length and penetration on welding parameters can be explained as follows. For a fillet weld [such as the one shown in Fig. 11(a)], the arc energy input is primarily responsible for the formation of the top part of the weld bead, whereas the volumetric heat source is largely responsible for the formation of the finger penetration (i.e., lower part of the weld bead). As the heat input per unit length increases, more base metal is melted in the weld cross section and the leg length thus increases. On the other hand, the dimensions and the power density of the volumetric heat source are more sensitive to the welding current. Therefore, as the welding current arises, the penetration also increases. As for the actual throat, it can be approximately determined from a combination of the leg length and penetration based on geometric consideration. Hence, the actual throat is resulted from a combination of the heat input per unit length and current.

As shown in Figs. 12 and 13, the average difference between the calculated and the measured values for the leg length, the penetration and the actual throat were found to be

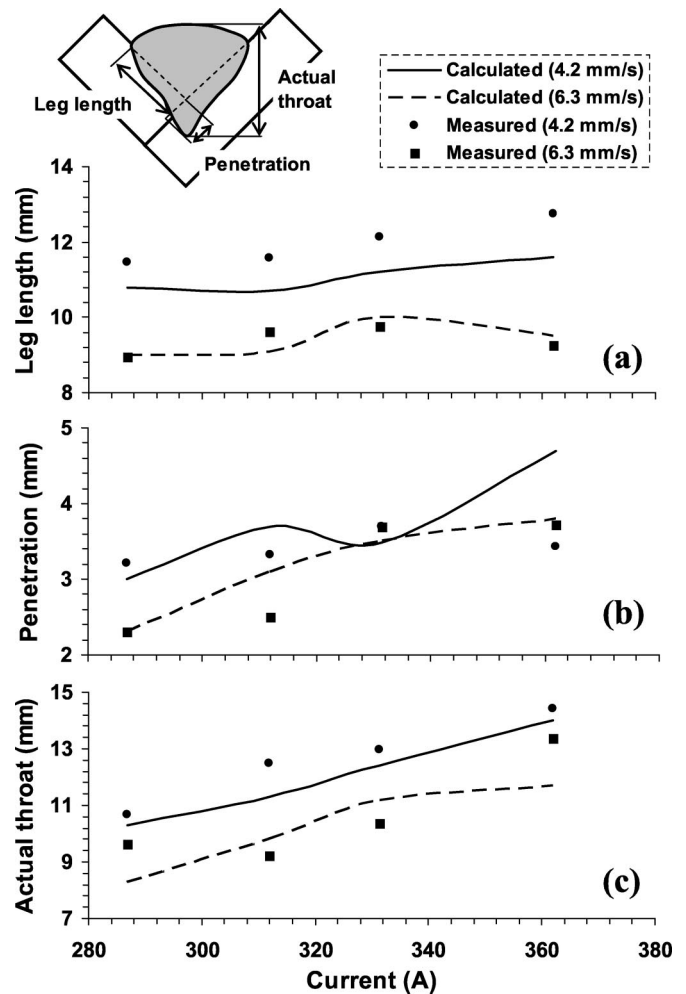


FIG. 12. Weld bead geometric parameters as a function of the current and welding speed: (a) leg length, (b) penetration, and (c) actual throat.

5.5%, 9.5%, and 8.0%, respectively. These numerical values are to be interpreted with caution because of the limited volume of experimental data and lack of any statistically significant index of the quality of the experimental data. In summary, the trends and values of the geometric variables of the fillet weld could be satisfactorily predicted by the numerical heat transfer model within the range of values of the welding variables investigated.

### III. SUMMARY AND CONCLUSIONS

A three-dimensional numerical heat transfer and fluid flow model was developed to calculate the temperature profiles, velocity field, weld pool shape and size, and the nature of the solidified weld pool reinforcement surface during GMA welding of fillet joints. The numerical model solves the continuity, momentum conservation, and energy conservation equations in a boundary fitted coordinate system, considering the free surface deformation, filler metal addition, and sensible heat input from the metal droplets. The details of the numerical model are available in part I of this article. The model was used to study GMA fillet welding of A-36 steel. The following conclusions can be drawn from the results.

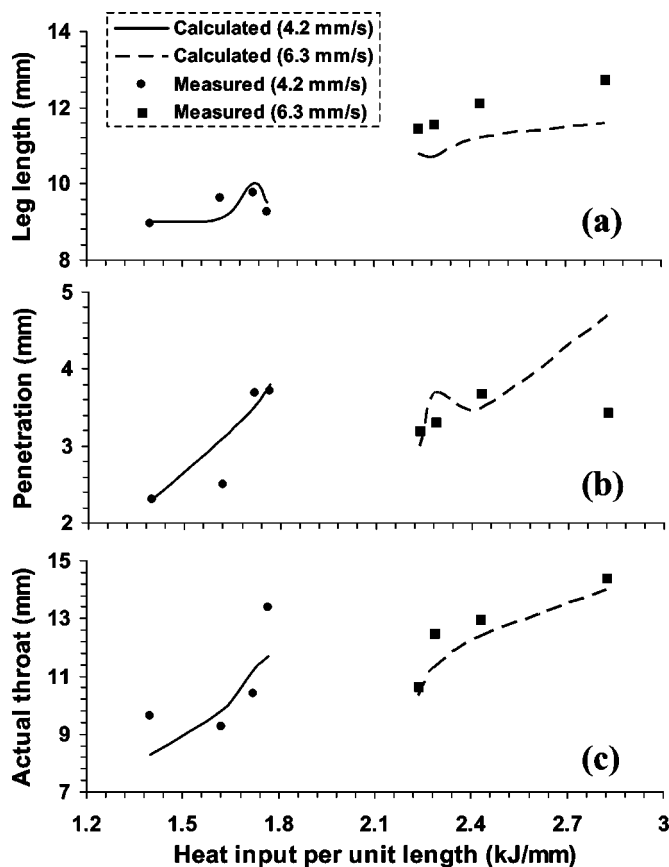


FIG. 13. Weld bead geometric parameters as a function of the heat input per unit length and welding speed: (a) leg length, (b) penetration, and (c) actual throat.

(1) The liquid metal convection plays dominant role in dissipating the heat in the weld pool. The melt convection determines the temperature distribution and shape of the weld pool. Heat transfer and fluid flow calculation results in not only a more realistic description of the heat transfer process in the weld pool but also provides a better agreement with the experimental weld bead profile than the heat transfer calculation alone.

(2) The role of various driving forces for the liquid metal convection was examined using both the dimensionless analysis and the numerical model. It is found that the liquid metal is driven mainly by the electromagnetic force

and the Marangoni shear stress and, to a much less extent, by the buoyancy force. The flow pattern resulted from different driving forces in fillet welds is similar to that in butt welds.

(3) Both the experimental results and the model predictions indicate that the average cooling rate between 1073 and 773 K decreased with increase in heat input per unit length. The calculated cooling rates were also in good agreement with independent experimental data.

(4) The numerically computed fusion zone geometry, finger penetration characteristic of the GMA welds and the solidified surface profile of the weld reinforcement were in fair agreement with the experimental results for various welding conditions. The leg length, penetration, and actual throat were found to increase with the increase in welding current. All these parameters decreased with the increase in welding speed. The predicted values of these three geometric parameters agreed well with those measured experimentally.

#### ACKNOWLEDGMENTS

The work was supported by a grant from the U.S. Department of Energy, Office of Basic Energy Sciences, Division of Materials Sciences, under Grant No. DE-FG02-01ER45900. W.Z. gratefully acknowledges the award of a Fellowship from the American Welding Society. The authors would like to express their gratitude to M. A. Quintana of Lincoln Electric Company and Dr. S. S. Babu of Oak Ridge National Laboratory for their interest in the work and for the experimental data. Valuable critical comments from Dr. A. De, Y. Fan, X. He, A. Kumar, and S. Mishra are appreciated.

<sup>1</sup>J. F. Lancaster, *The Physics of Welding*, 2nd ed. (Pergamon, Oxford, 1986).

<sup>2</sup>S. A. David and T. DebRoy, *Science* **257**, 497 (1992).

<sup>3</sup>T. DebRoy and S. A. David, *Rev. Mod. Phys.* **67**, 85 (1995).

<sup>4</sup>C.-H. Kim, W. Zhang, and T. DebRoy, *J. Appl. Phys.* **94**, 2667 (2003).

<sup>5</sup>M. C. Tsai and S. Kou, *Weld. J. (Miami, FL, U. S.)* **69**, 241s (1990).

<sup>6</sup>X. He, P. W. Fuerschbach, and T. DebRoy, *J. Phys. D* **36**, 1388 (2003).

<sup>7</sup>W. Zhang, G. G. Roy, J. W. Elmer, and T. DebRoy, *J. Appl. Phys.* **93**, 3022 (2003).

<sup>8</sup>P. Sahoo, T. DebRoy, and M. J. McNallan, *Metall. Trans. B* **19B**, 483 (1988).

<sup>9</sup>W. Pitscheneder, T. DebRoy, K. Mundra, and R. Ebner, *Weld. J. (Miami, FL, U. S.)* **75**, 71s (1996).

<sup>10</sup>W. Zhang, J. W. Elmer, and T. DebRoy, *Mater. Sci. Eng., A* **333**, 320 (2002).

<sup>11</sup>S. Kou, *Welding Metallurgy*, 2nd ed. (Wiley, New Jersey, 2003).

<sup>12</sup>G. M. Oreper and J. Szekely, *Metall. Trans. A* **18A**, 1325 (1987).

<sup>13</sup>K. Masubuchi, *Analysis of Welded Structures* (Pergamon, Oxford, 1980).